Multilayer GZ/YSZ thermal barrier coating from suspension and solution precursor thermal spray

K. Leng [*], A. Rincon Romero, T. Hussain

Coatings and Surface Engineering, Faculty of Engineering, University of Nottingham, NG7 2RD, United Kingdom

ARTICLE INFO

ABSTRACT

Rare-earth (RE) zirconates, such as gadolinium zirconate (GZ), gained much attraction to be used for the next generation TBC. A double-layer and triple-layer TBC were deposited using the suspension and solution precursor high velocity oxy fuel (HVOF) thermal spray. A dense solution precursor GZ layer was intended to minimise the crack propagation from underneath, thereby inhibiting the CMAS infiltration. In the furnace cycling test, the double- and triple-layer coatings had a comparable cyclic lifetime. For the CMAS test, both the double- and triple-layer coatings were exposed to CMAS at 1250 °C for 30 mins. The CMAS deposits melted and infiltrated both coatings through the dense vertical cracks (DVCs). Interestingly, the GZ reacted with the molten CMAS to form a gadolinium apatite phase ($Ca_2Gd_8(SiO_4)_6O_2$) that was detected in the double- and triple-layer TBC. Both the double- and triple-layer TBCs succeeded in reacting with CMAS.

1. Introduction

Thermal barrier coatings (TBCs) have been successfully employed in turbine engines since the 1970s [1]. The TBC system aims to protect the underlying metallic substrates (i.e., nickel-based superalloys) from the harsh environment, resulting in an increase in the lifetime of the turbine blades and allows to operate at a higher temperature. The higher operating temperature increases the efficiency of the turbine engine, thereby reducing the overall greenhouse gas emissions [1,2].

A typical TBC consists of the substrate, the bond coat, either the MCrAlY (M = Co, Ni, or Fe) alloys or Pt/Ni-rich aluminide [3], and the topcoat. The MCrAlY alloy, which functions to protect the metallic layer underneath and minimise the thermal expansion mismatch between the substrate and topcoat, is mainly deposited by either the low-pressure plasma spray (LPPS) or the high velocity oxy-fuel (HVOF) thermal spray. The widely used topcoat, 7–8 wt% yttria stabilised zirconia (YSZ), which has been established for many decades, suffers a phase transformation at around 1200 °C [4,5]. Beyond this operating temperature, the YSZ will transform from the metastable tetragonal (t′) phase into the tetragonal (t) phase and subsequently to the monoclinic (m) and cubic (c) phase. As a result, high-level stress will be introduced into the microstructure of the topcoat as this transformation is associated with 3–5% volume change, resulting in a catastrophic failure [6]. In addition to that, the YSZ is susceptible to CMAS (Calcia-Magnesia-Alumina-Silicate) attack at high temperatures (i.e., > 1200 °C), which significantly reduces the lifetime of the TBC. Therefore, the rare-earth (RE) zirconates, typically gadolinium zirconate (GZ), gained attention to overcome these drawbacks. GZ has the potential to react with CMAS to form an apatite phase ($Ca_2Gd_8(SiO_4)_6O_2$) that prevents the infiltration of the molten CMAS through the topcoat [6–10]; however, due to the poor mechanical properties, GZ can only be used in a multilayer approach (i.e., double layer), as already been proposed in several studies [11–16].

Nowadays, TBCs are mainly produced by the atmospheric plasma spray (APS) method and the electron physical vapour deposition (EB-PVD) method. The coatings produced by the APS process can be varied from a lamellar to a dense vertically crack (DVC) microstructure depending on the spray conditions or parameters [4,10,17–24], whereas the EB-PVD process will only produce the typical columnar microstructure [25–27]. Other thermal spray methods, such as the suspension or solution precursor plasma spray (SPS/SPPS) and suspension or solution precursor HVOF (S-HVOF/SP-HVOF), are gaining more attention in the development of TBCs although it is not fully implemented in the industry due to costs associated with capital investment, limited feedstock supply chain and technology readiness level. Both thermal spray methods provide a high degree of freedom in producing a desired doped or un-doped coating composition with the purpose of overcoming the shortcomings of current thermal sprayed TBCs. Moreover, both methods

---

---

can produce a wide range of coating structures varying from a lamellar to a columnar or a DVC structure, significantly affected by various factors like the surface tension of the liquid medium and the surface roughness of the substrate [28,29]. The parameters which can be optimised in these processes are significantly more than the conventional powder based thermal spray. In addition, the short spraying distance required by these methods remains a challenge to deposit TBCs onto a component with complex shapes. Recent studies showed that SPS can produce the columnar structures with a comparable lifetime with the EB-PVD TBCs [30–46] and S-HVOF thermal spray can produce DVC structures with superior mechanical properties.

Moreover, the solution precursor (SP) feedstock that can be produced through the mixing of solutes (salt) and solvents (water) could be used as an alternative to the suspension feedstock. Jiang et al. [47,48] produced a double-layer TBC with a DVC structure and layered porosity (inter-pass boundaries) through the solution precursor (SPPS GZ/SPPS YSZ) feedstock, which presented a promising thermal cyclic lifetime and CMAS resistivity. Kumar et al. [19] also studied the DVCs microstructure produced by the same method as Jiang et al. and compared it with the typical APS microstructure, the lamellar microstructure. Due to the presence of the DVCs in the SPPS coating, it functioned similar to the columnar structure which can accommodate the strain-tolerance in the coating during the thermal cycling test, thereby showing a good thermal cycling lifetime. Despite the good performance in the thermal cycling test, the DVCs or the columnar structured TBC coatings performed poorly in CMAS attacks [9,49–51]. The CMAS attack can be mitigated by selecting a CMAS resistant material and tailoring the microstructure of the coating. Wellman et al. [51] demonstrated that if the width of the columnar structure was less than 1 μm, the DVC or columnar structure could play an important role in successfully form a sealant layer that could stop CMAS from infiltrating further without compromising the stress-relieving structure (DVCs or columnar structure).

Compared with the traditional single-layer YSZ TBC, an improved durability in the furnace cycling tests (FCT) for the SPS double- and triple-layer TBCs was demonstrated by Mahade et al. [13,52]. The SPS double-layer TBC comprised of the SPS GZ and the SPS YSZ layer, while the triple-layer TBC had a dense SPS GZ layer being deposited on top of the SPS GZ layer. The dense SPS GZ layer was achieved by altering the spray parameter in both works. Although the triple-layer TBC had a slightly lower column density than the double-layer TBC, the columnar structure continued from the pre-existed layer (SPS GZ) to the dense SPS GZ layer. The presence of the columns or vertical cracks that could potentially act as a pathway for CMAS infiltration led to a further investigation.

From the previous work [53], it was demonstrated that the S-HVOF process is capable of producing the DVCs microstructure, while the solution precursor HVOF (SP-HVOF) creates a dense microstructure that seals or minimises the crack width of the DVCs structure from the previous layer. Although the double-layer coating (SP-HVOF GZ/S-HVOF YSZ) presented a similar coating lifetime to the traditional single-layer YSZ (S-HVOF YSZ) coating, the coating thickness was thinner than the conventional TBC thickness, ~ 400 μm [54]. Therefore, in this study, a double- and a triple-layer coating were designed and deposited through the HVOF thermal spray. It is worth noting that the scope of the study is mainly on the comparison between the two multilayer approaches, and the purpose is not to compare and contrast these coatings with a commercial YSZ coating. The double-layer coating was comprised of the YSZ and GZ layer deposited through the suspension feedstock, whereas the triple-layer coating had an additional dense GZ layer on top of the S-HVOF GZ layer. The dense GZ layer (SP-GZ) was deposited with a solution precursor feedstock [47,53]. The primary purpose of this study was to design an architecture that could resist CMAS attack, in the meantime, without compromising the stress-relieving cracks that are proven to be beneficial to the thermal cycling lifetime of a TBC. The dense SP-GZ layer aims to seal or minimise the DVCs structure developed from the previous layer, either by reducing the open cavities for

molten CMAS or minimising the width of DVCs that could ease sealing the stress-relieving cracks.

2. Experimental methods

2.1. Substrate and bond coat preparation

Inconel 718 disc-shaped substrates of 12.7 × 3 mm dimension and nominal composition of Ni-19.0Cr-3.0Mo-5.1Nb-0.5Al-0.9Ti-18.5Fe-0.04C (in wt%) were grit blasted (Guyson, Dudley, UK) with fine F100 brown alumina (0.125 – 0.149 mm) particles at 6 bars. All grit blasted substrates were sonicated in Industrial Methylated Spirit (IMS) using an ultrasonic bath for up to 4 min to remove loose alumina particles and subsequently were blown dry with compressed air. The Co-based bond coat, CoNiCrAlY powder (CO-210–24, Praxair, Swindon, UK), was deposited on all grit-blasted substrates with High Velocity Oxy-Fuel (HVOF) thermal spray using the commercial MetJet IV (Metallisation, Dudley, UK) gun [55]. The gun was mounted on a 6-axis robot (ABB® IRB 2400, Warrington, UK) that provides a standard raster scan pattern. The scanning speed was set at 1000 mm/s with a line spacing of 4 mm to factor in the nozzle diameter. A detailed deposition of the bond coat was described by Saeidi et al. [55]. All substrates were bond-coated in the same batch at a thickness value of ~110 μm.

2.2. Suspension and solution precursor preparation

Two ethanol-based suspensions were provided by Treibacher Industrie AG (Althofen, Austria). The suspensions comprised of 8 wt% yttria stabilised zirconia (AuerCoat YSZ) and gadolinium zirconate (AuerCoat Gd-Zr) with a median particle size (D_{50}) of 0.45 and 0.50 μm, respectively. Before the deposition, both suspensions were placed on a roller (Capco, Suffolk, UK) for 1 h at 50 rpm, then transferred to a pressurised feeder with continuous stirring to obtain a well-dispersed suspension. According to the supplier, both suspensions had a solid loading of 25 wt%.

The dense layer gadolinium zirconate (GZ) layer was deposited with a solution precursor (SP) feedstock. The SP feedstock was prepared following the method described in the previous work [53], using gadolinium nitrate (III) hexahydrate (Fisher Scientific, Loughborough, UK) and zirconium acetate (Sigma Aldrich, Dorset, UK) in a stoichiometric proportion. The ceramic yield of the solution precursor was 10 wt%.

2.3. Topcoat deposition

Two different variations in TBCs comprising of double-layered and triple-layered ceramics, as shown in Fig. 1, were deposited with a modified GTV SS-TopGun torch mounted on the robot mentioned above. The details of the torch can be found somewhere else in [53,56]. The spray parameters are listed in Table 1.

2.4. Material characterisation

An aliquot of the YSZ and GZ suspension was dried in a box furnace at 200 ºC for 1 h to obtain a sample of dried powders. The phase identification of the dried feedstock powder, as-sprayed and failed TBCs was performed using a D8 Advance DaVinci system (Bruker, Coventry, UK), equipped with a lynx eye detector. The diffractograms were obtained with Cu-Kα radiation with a wavelength of 1.54 Å in Bragg-Brentano scanning mode. The scanning range began from 10° to 90° using a 0.02° step size and a counting time of 0.2 s in each step. The phase identification was performed using the DIFFRACT.SUITE EVA software (Bruker, Coventry, UK).

Both the as-sprayed and failed TBCs were cold-mounted in epoxy resin and hardener (Struers, Denmark) through vacuum impregnation. A SiC precision cut-off wheel (MetPrep, Coventry, UK) was used to cross-section the sample. A slow cutting speed (0.01 mm/s) was employed to
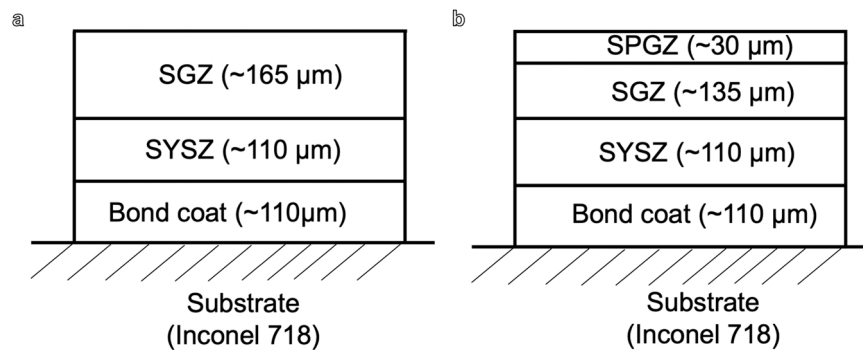
Fig. 1. (a) A schematic diagram of the double-layered coating and (b) the triple-layered coating in this study, where 'S' stands for suspension and 'SP' stands for solution precursor. Both coatings had the same substrate, Inconel 718.

Table 1
Spray parameters used to deposit the double- and triple-layered TBCs. [53].

Parameters	Suspension Yttria Stabilized Zirconia	Suspension Gadolinium Zirconate	Solution Precursor Gadolinium Zirconate
Torch	Suspension TopGun	Suspension TopGun	Suspension TopGun
H_2 flow rate (L/ min)	700	700	614
O_2 flow rate (L/ min)	300	300	307
Stand-off distance(mm)	85	85	85
Scan speed (mm/s)	1000	1000	1000
Scan line distance (mm)	3.5	3.5	3.5
Nozzle length (mm)	22	22	22
Suspension flow rate (mL/min)	40	40	40
Flame power (kW)	99	99	101
Number of passes	50	50	50

complete the cutting process as the samples were sensitive to cutting. The sectioned samples were sequentially grounded with SiC grinding papers (MetPrep, Coventry, UK) and polished to a surface finish of 1 μm by diamond polishing.

To observe the dried suspension powders, the as-sprayed coating structures and the failure mode of TBCs after thermal cycling and CMAS tests, scanning electron microscope (SEM) images were taken using JSM-6490LV (JEOL, Massachusetts, USA). All images were taken with a spot size of 50 nm, a working distance of 10 mm and an acceleration voltage of 15 kV. The coating thickness was measured by taking the average of 10 measurements on secondary electron images (SEI) at a magnification of x300, covering approximately 1 cm of the coating cross-section with 5 images. The porosity was calculated by taking the average measurement of three backscattered electron (BSE) images at a magnification of x300, converting the image to a black and white (8 bits) map upon setting a threshold and measure the area percentage of the image covered by porosity using the "analyse particle" automated function. Both the coating thickness and porosity measurement were done using the open-source software, ImageJ (NIH, USA), with standard error being calculated and reported. Buehler 1600 Series Micro-hardness Tester (Illinois Tool Works, USA) was used to measure the micro-hardness on each layer of the polished coating cross-section. A 50-gf load was chosen to create a clear indentation, ensuring no cracks propagated from the indented area.

For a better BSE imaging, Quanta 600 (FEI Europe, Netherlands) was

employed to map the CMAS infiltrated region through Ca and Si mapping. An acceleration voltage of 20 kV, a spot size of 50 nm, and a working distance of 13 mm were used. The CMAS infiltrated region was defined as the area where CMAS could be detected, through Ca and Si mapping or BSE imaging.

2.5. Crack density measurement

A horizontal straight line of known length was drawn on the cross-sectional SEM micrographs at x200 magnification in each layer. All cracks intersecting the line were considered. The crack density was calculated using the equation below [57]:

$$Crack density\left(\frac{cracks}{mm}\right) = \frac{No. of cracks intercepted the line}{True length of the line}$$

A total of 10 micrographs of the same magnification were measured and the average value is reported.

2.6. Thermal cycling test

Three samples of each type, including the commercial aerospace APS standard single-layered YSZ coatings, were subjected to thermal cycling tests. All samples were heat-treated at 1135 °C for 2 h at a ramp rate of 5 °C/min to burn all residues that may be left in the coating. A cycle of the thermal cycling test comprised of a heating stage, which heated the samples to 1135 °C in 10 min, a dwelling stage, which held the samples at 1135 °C for 45 min, and a cooling stage, which cooled the samples through forced air-cooling below 100 °C in approximately 30 min using a programmable bottom-loading isothermal furnace (CM Furnaces Inc., Bloomfield, USA). The test was constantly monitored with a high-definition Webcam (Logitech C930e) by capturing an image every 1 min interval. The sample is considered as failed when the spallation area of TBCs is more than 20%.

2.7. CMAS test

CMAS powder (Oerlikon Metco, Cheshire, UK) with a nominal composition of $35CaO-10MgO-7Al_2O_3-48SiO_2$ in mol% was initially mixed with deionised (DI) water in a 1:9 ratio by weight and homogenised using a stirrer for 10 min to form the CMAS aqueous solution. The CMAS concentration was chosen according to OEM protocol, guidance from the high temperature community [58]. The surface area and the initial mass of the sample were measured before CMAS deposition to ensure that 15 mg/cm^2 of CMAS was successfully deposited on each sample. During CMAS deposition, the CMAS aqueous solution was constantly stirred on an Isotemp hot plate (Fisher Scientific, Loughborough, UK) at 60 °C whereas the sample was placed on a hot plate at approximately 100 °C to evaporate the DI water contained in the solution. An air brush kit was used to deposit the CMAS uniformly on top of

the sample. The sample was weighted again as soon as the water had completely evaporated. This process was repeated until the desired concentration was achieved.

The CMAS-coated samples were heat-treated at 1250 °C for 30 min, at a ramp rate of 10 °C/min, in a BRF14/5 box furnace (Elite Thermal Systems Ltd., Leicester, UK). The same ramp rate was set to cool down the furnace to 1000 ºC, and a ramp rate of 5 ºC/min was set to cool the furnace to room temperature. The controlled cooling rate was set to reduce the thermal shock behaviour in the samples. All samples were placed on top of an alumina plate to avoid any reaction between the sample and the furnace.

3. Results

3.1. Feedstock and coating characterisation

Both feedstock powders, YSZ and GZ, are shown in Fig. 2. The dried particles of both YSZ and GZ powders showed mostly irregular powder morphology. The particle size distribution of the YSZ and GZ suspensions are shown in Figs. 3(a) and 3(b) respectively. The particles in the YSZ suspension had a median size (D_{50}) of ~ 0.52 µm, D_{10} of ~ 0.29 µm and D_{90} of ~ 0.97 µm, whereas the GZ suspension had a median size (D_{50}) of ~ 0.50 µm, D_{10} of ~ 0.26 µm and D_{90} of ~ 0.99 µm.

As mentioned in the Experimental method section (Section 2.3), two types of coatings were produced in this study: a double-layered and a triple-layered coating. Figs. 4(a) and 4(b) show SEM micrographs for the two coating microstructures. A higher magnification image of these coating microstructures is shown in Figs. 4(c) and 4(d). All samples were coated with a bond coat with a thickness of 102 ± 4 µm. in the same spray run to avoid any run-to-run variation.

In the double-layered coating, the topcoat suspension YSZ (S-YSZ) layer had an average thickness of 110 ± 3 µm and the suspension GZ (S-GZ) layer had an average thickness of 165 ± 4 µm; while in the triple-layered coating, the topcoat S-YSZ layer had an average thickness of 115 ± 3 µm, the S-GZ layer had an average thickness of 135 ± 3 µm and the solution precursor GZ (SP-GZ) layer had an average thickness of 30 ± 2 µm. Both samples (double- and triple-layer coatings) had the same total thickness of approximately 385 µm. The thermal characteristics of the SP-GZ feedstock to form the GZ phase was discussed in the previous work [53]. Both the as-sprayed double- and triple-layered coating structures were relatively dense, containing 5 ± 1% porosities in each layer. Moreover, the microhardness value in the S-YSZ and SP-GZ was similar while the S-GZ had the highest value, as shown in Table 2.

From the higher magnification SEM images (Fig. 5), each layer presented uniformly disturbed micropores. Comparing the as-sprayed condition of each layer, the vertical cracks initiated from the S-YSZ

layer continued to propagate to the S-GZ layer and the SP-GZ layer. In the triple-layer coating (Figs. 4b and 4d), the vertical cracks were seen to narrow down or stop propagating in the SP-GZ layer. Interestingly, the S-GZ layer in both the samples (double- and triple-layer coatings) was observed with the existence of horizontal cracks branching out from the vertical cracks. The horizontal cracks phenomena seen in the S-GZ layer were believed to be corresponded to the low fracture toughness properties of GZ. The branching cracks showed that the differential strain in the S-GZ layer was sufficient to cause an interfacial cracking [59]. The micropores or microcracks in the vicinity of the DVCs that existed in the S-GZ layer may provide a path for these cracks to propagate laterally.

Comparing both the as-sprayed coatings, the double-layered coating had a more pronounced vertical crack density than the triple-layered coating, with a crack density of 10.0 ± 1.0 mm^{-1} and 5.5 ± 0.5 mm^{-1}, respectively. It was worth noticing that the vertical cracks in the double-layered structure initiated after depositing ~ 40 µm of S-YSZ; however, this was not the case for the triple-layered coating (Figs. 4b and 4d). As seen in the triple-layered coating, the difference in the vertical crack propagation was believed to occur after depositing the additional dense layer, SP-GZ. On the other hand, no apparent pores or gaps were seen at the interface of each layer, evidencing a good adhesion in each layer of both coating structures.

3.2. X-ray diffraction of coatings

The combined XRD patterns of the S-YSZ powder and as-sprayed S-YSZ coating are presented in Fig. 6(a). The XRD peaks showed that the as-received suspension had the tetragonal YSZ (PDF Card #048–0224) as the main peaks, with a small amount of monoclinic zirconium oxide (PDF Card #078–0047); however, the monoclinic zirconium oxide phase was no longer observed in the as-sprayed SHVOF YSZ coating. The diffractogram only detected the peak of the tetragonal YSZ. The absence of the monoclinic phase in the as-sprayed coating suggested that the in-flight particles underwent rapid cooling (i.e., ~ 10^6 Ks^{-1} or greater [60]) upon impact onto the substrate, resulting in the monoclinic or cubic phase transformation of zirconia was not possible to occur in the as-sprayed coating.

The diffractogram in Fig. 6b represented the peaks of the dried S-GZ and SP-GZ powders as well as the SHVOF GZ and SPHVOF GZ as-sprayed coatings. The dried S-GZ powder had the cubic fluorite GZ (PDF Card #080–0471) as the main peaks. A low intensity of pyrochlore GZ (PDF Card #080–0470) was detected in the as-received suspension; however, it was noticed that the pyrochlore GZ phase disappeared in the SHVOF GZ coating. The absence of pyrochlore GZ phase in the as-sprayed coating, either the SHVOF or SPHVOF GZ, was attributed to the rapid solidification of the molten splats as soon as it impacted onto the
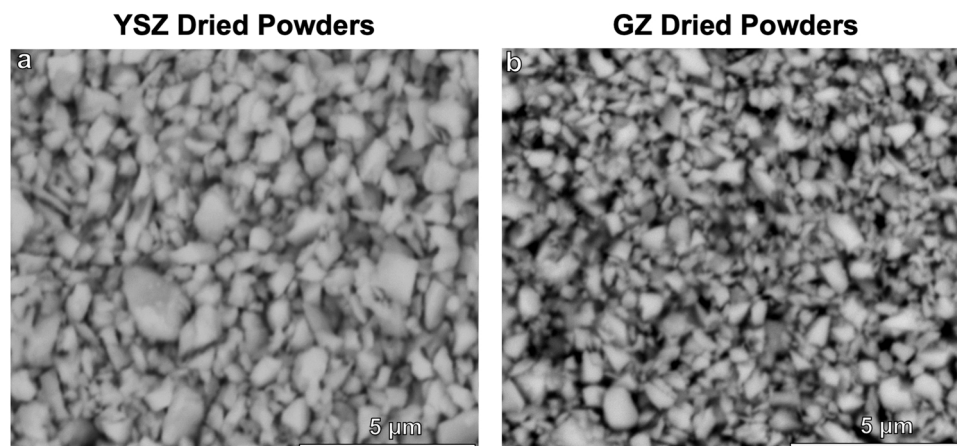
YSZ Dried Powders   **GZ Dried Powders**

Fig. 2. (a) The back-scattered (BSE) image of the YSZ dried powders, and (b) the GZ dried powders showing that both powders are mainly comprising of irregular morphologies.
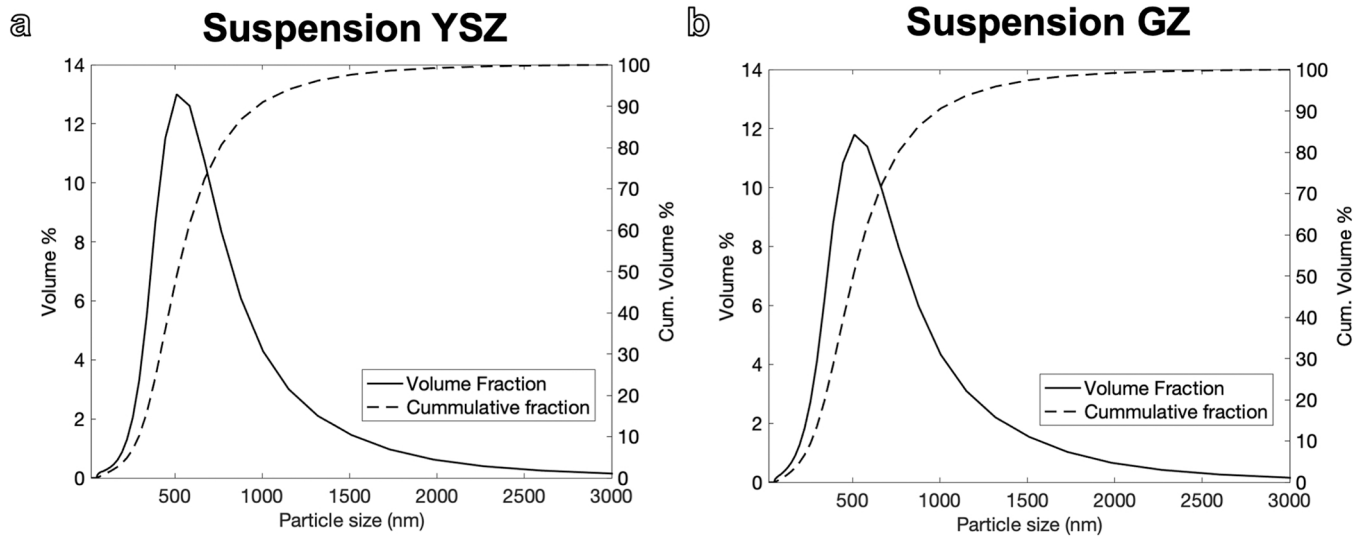
Fig. 3. Particle size distribution profile of (a) YSZ and (b) GZ particles in the supplied suspension. Continuous lines represented the volume fraction whereas the dashed lines represented the cumulative fraction.
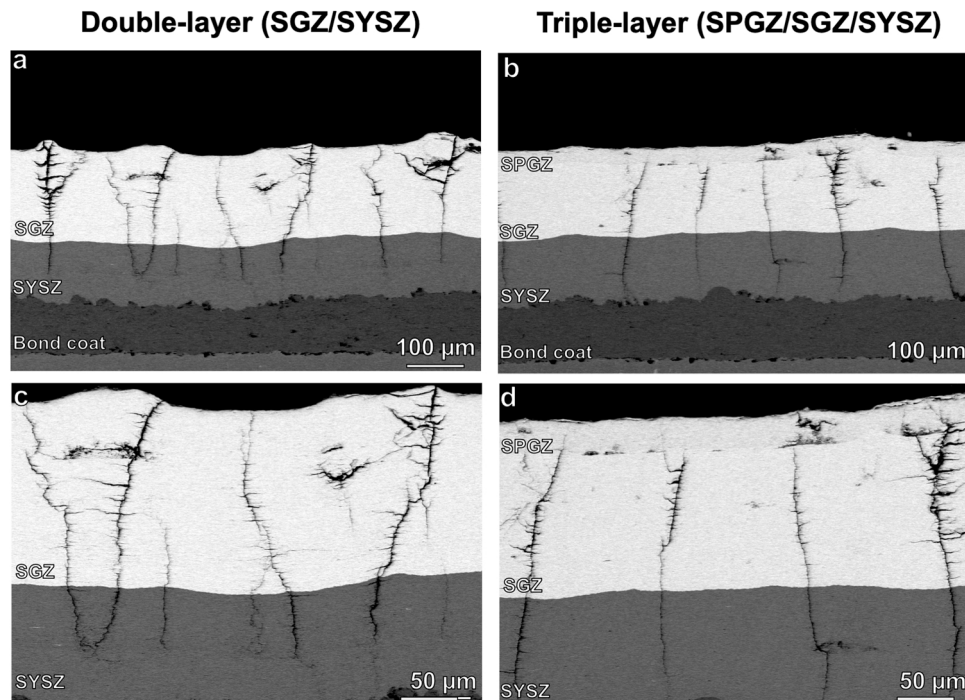

Fig. 4. (a) A backscattered (BSE) image of the double-layered coating, and (b) tri-layered coating. (c) and (d) shows the high magnification of each coating structure respectively.

Table 2
shows the mechanical properties of the *coating structure in each layer.*

Layer	Microhardness, $Hv_{0.5}$
SP-GZ	504 ± 20 Hv
S-GZ	583 ± 23 Hv
S-YSZ	524 ± 31 Hv

substrates. The formation of the pyrochlore GZ phase only occurs with an equilibrium cooling below 1550 ºC [61,62].

To obtain the dried SP-GZ powders, the SP feedstock was heat-treated at 1400 °C for 2 h. The diffractograms of the dried SP-GZ powder and as-sprayed SPHVOF GZ coating only showed the cubic fluorite GZ (PDF Card #080–0471). This evidenced that the chosen flame power was sufficient to evaporate the solution and melt the in-flight GZ particles. A more detailed work can be found in [53].

3.3. Furnace cycling test (FCT)

From the histogram plot (Fig. 7), the double-layered is observed to have a longer thermal cycling lifetime than the triple-layered coating. The life cycle for the double-layered coating is 74 ± 13 cycles and for the triple-layered coating is 55 ± 4 cycles.

The cross-sectional SEM micrographs of the failed samples are shown in Fig. 8. The double- and triple-layered samples failed at the TGO/
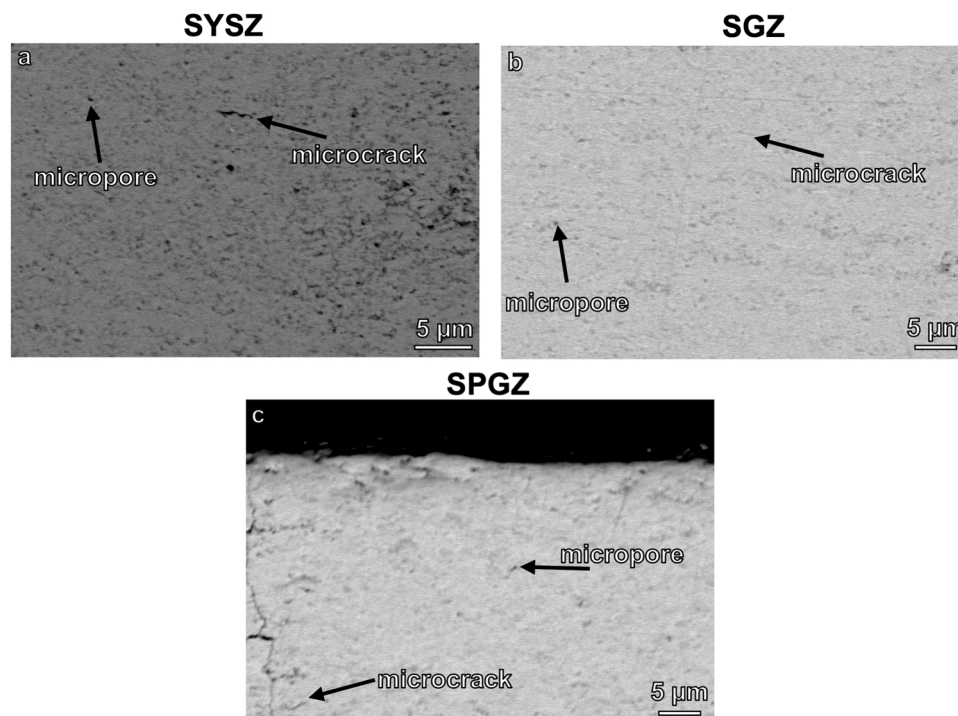
SYSZ

SGZ

SPGZ

Fig. 5. (a) High magnification BSE images of the SYSZ layer, (b) SGZ layer and (c) SPGZ layer. All three layers presented a uniformly distributed micropores throughout the cross section.

topcoat interface. Dense vertically cracks that were already formed in both the as-sprayed coatings propagated through the entire thickness of the coating and subsequently widened. Horizontal cracks were also seen to initiate and propagate laterally in both the samples; however, the widening of vertical cracks and the propagation of horizontal cracks were more pronounced in the double-layered sample (Fig. 8a). The difference in the crack propagation phenomena between the double- and triple-layered samples may be related to the longer life cycle of TBCs in the thermal cycling furnace. Although some horizontal cracks were seen to intersect with the adjacent vertical crack, the propagation of these lateral cracks did not cause the TBC to spall off from the substrate. In fact, most horizontal cracks were observed to propagate within the layer, either S-YSZ or S-GZ layer. It was worth noticing that most horizontal cracks in the S-YSZ layer were initiated at the region near to the TGO/topcoat interface.

Moreover, the TGO thickness for both samples are approximately 6 µm, as seen in Fig. 9. In the previous work, Mahade et al. [63] reported that the spallation of TBC occurred after reaching a critical TGO thickness of 5 µm, whereas Lu et al. [24] reported a TGO critical thickness of 7 – 8 µm. It could be concluded that the TGO critical thickness to the spallation of TBC is likely dependent on the composition of the bond coat. Furthermore, EDX analysis on the bond coat before and after thermal cycling tests (Table 3) showed that the nominal aluminium (Al) composition throughout the bond coat thickness decreased from 9 wt% (before thermal cycling) to 4.5 wt% (after thermal cycling), indicating the outward diffusion of Al. The outer bright layer being spinel, comprised of Cr, Co and Ni; the inner layer being the α-Al$_2$O$_3$.

3.4. CMAS test

The CMAS composition used has a glass transition temperature of $\sim$ 800 ºC and a melting temperature of $\sim$1220 ºC, determined by the TGA/DSC measurements (not shown here). The CMAS is expected to be fully molten with an exposure temperature of 1250 °C. The area concentration used here is well above the minimum requirement for CMAS to fully infiltrate the TBCs, subsequently to the failure of TBCs [51].

The cross-section of the 0.5 h CMAS exposed samples can be seen in Fig. 10. Both the double- and triple-layered coatings are observed to fail from CMAS infiltration. The GZ layer in both coating structures had disappeared, which can be seen more prominently in the triple-layer coating structure (Fig. 10b). The vertical cracks in the as-sprayed YSZ layer (Figs. 4a and 4b) are shortened, and most of the horizontal cracks in the as-sprayed GZ layer (Figs. 4a and 4b) had disappeared. These may be sealed by the reactant products between the coating and CMAS. Although both coatings failed from CMAS infiltration, no apparent lateral cracks were seen to propagate through the topcoat interface (GZ/YSZ). Besides, a thin TGO layer is also observed in the double- and triple-layered samples; however, the TGO was not the primary reason the samples failed. The TGO thickness is well below the critical thickness, $\sim$ 5.5 µm, as the samples were only exposed for 0.5 h at 1250 °C.

According to the XRD phase analysis as shown in Fig. 11, a small amount of gadolinium apatite (Gd$_8$Ca$_2$(SiO$_4$)$_6$O$_2$) phase was detected in both the double- and triple-layered coating structures. In the case of the triple-layered coating, a significant reduction in the intensity of GZ is observed, supported by the BSE micrograph in Fig. 10b. The tetragonal YSZ peaks were detected as the prominent peaks because the GZ layer was partially lost after the CMAS infiltration. The GZ layer experienced a thermal shock phenomenon during the cooling stage, exposing the layer underneath it, the YSZ layer.

The finding of the XRD peaks is supported by the elemental map depicted in Fig. 12. From the elemental map, the CMAS infiltrated both coating structures through the strain-tolerant vertical cracks. A high contrast of Ca and Si maps is detected around the vertical cracks. From the Si map, it is noticed that Si reacts more readily with YSZ than with Ca. The Ca is seen to stop at the GZ/YSZ interface. For the GZ layer, needle-like structures are observed (Fig. 12c). These needle-like structures are expected to be the gadolinium apatite, supported by the high contrast of Gd, Ca and Si maps; however, the gadolinium apatite crystallisation did not stop the CMAS from infiltrating the TBC samples.
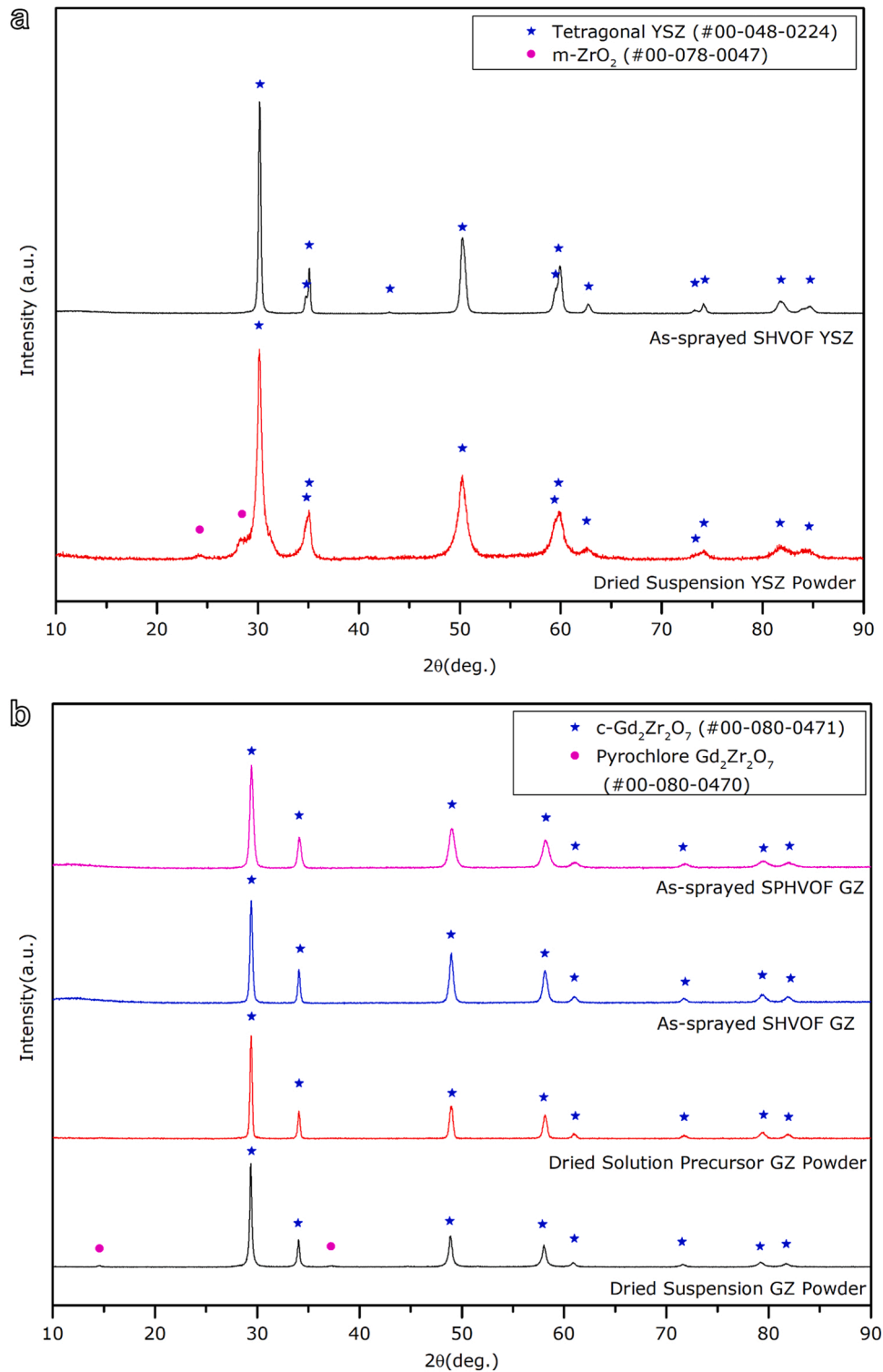
Fig. 6. (a) The XRD peaks of the dried SYSZ powder and SHVOF as-sprayed YSZ layer. (b) The XRD result of the dried SGZ and SP GZ powder and the as-sprayed coating of SHVOF GZ and SPHVOF GZ.

4. Discussion

4.1. Microstructure of the as-sprayed coatings

The results above showed that the as-sprayed HVOF thermal spray coatings had the typical DVCs structure necessary for strain tolerance. The coating microstructure is observed to be similar between the double- and triple-layer coatings. As mentioned above, all samples were produced in the same spray run. Therefore, it can be concluded that the variation in DVCs observed in the triple-layer coating is believed to occur during the deposition of the last layer, the SP-GZ layer.

The formation of DVCs in HVOF thermal spray is mainly due to the rapid solidification of molten splats. Upon impacting onto the substrates, the molten splats of the sprayed materials (i.e., YSZ and GZ) underwent rapid cooling and solidified to form the deposited coating. These phenomena lead to a high quenching stress in the 'freshly'
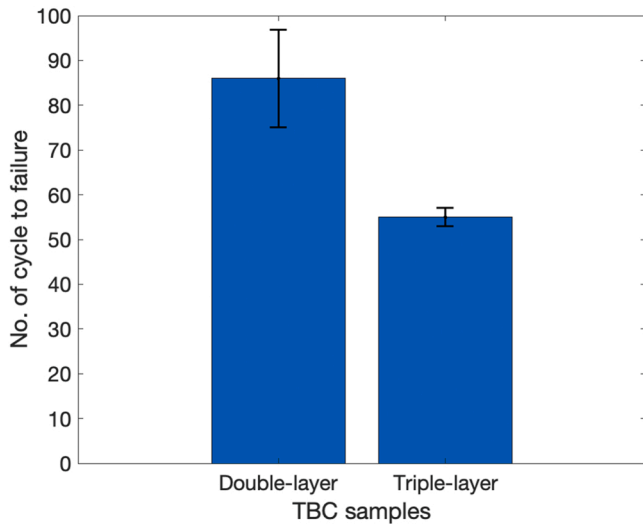
Fig. 7. Thermal cycling life of TBC samples, comprising of the double- and triple-layered coating. 3 samples for each condition were tested.

deposited coatings [43]. As the deposition pass increases, the stress accumulation in the coating is expected to increase significantly. Other factors such as the substrate temperature may also contribute to the stress increment in the deposited coating. Reported by Shinde et al. [23], APS coatings with segmentation cracks had a substrate temperature in the range of 400–450 °C during deposition. In the double-layered sample, the DVCs are observed to initiate after depositing ∼ 40 μm of the S-YSZ layer. It can be explained that the accumulated stress during deposition exceeds the yield strength of YSZ, leading to the nucleation and propagation of vertical cracks in the subsequent passes. A similar observation was also reported by Shinde et al. where segmentation

cracks in APS coatings were formed after the deposited coatings had built up to a certain extent [23].

For the triple-layered sample, the DVCs in the pre-existing layers (SGZ/SYZ) are observed to have extended towards the bond coat. The pre-existing two layers (SGZ/SYZ) can experience to a certain extent heat-treatment arising from the deposition of the dense SP-GZ layer. As explained by Shinde et al. [23], the elastic modulus of the deposited coating is on a near-linear dependence to the substrate temperature during deposition. Although the flame power utilised for the SP-GZ was slightly higher than the suspension feedstocks, the change in the deposition condition such as the substrate temperature per pass may be significant in the stress accumulation within the 'freshly' and pre-deposited coatings; however, a more extensive study in the deposition condition relative to the spray parameter is required.

On the other hand, the microstructure of the SP GZ layer is different to the pre-existing layers although DVCs are observed to continue in the SP GZ layer. The denser microstructure might be attributed to the utilisation of SP feedstocks, resulting in a finer molten splat deposited onto the substrates [64]. As studied by Govindarajan et al. [65], it was

Table 3

EDX analysis of bond coat before and after thermal cycling tests *(in wt%)*.

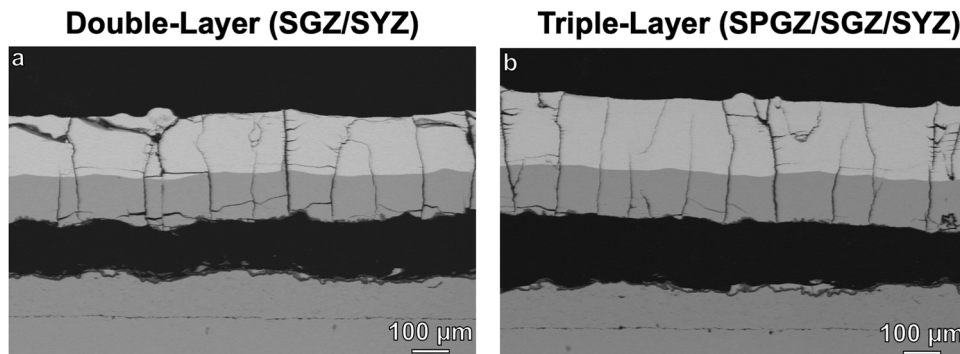| Elements	Before thermal cycling		After thermal cycling			
	1	2	3	4	5	6
O	0.6	1.4	35.3	51.1	2.1	-
Al	9.5	9.2	15.1	48.9	4.6	4.0
Y	0.5	0.7	-	-	-	-
Ti	-	-	-	-	0.3	0.4
Cr	21.4	21.3	21.3	-	21.2	20.8
Fe	-	-	-	-	4.5	7.0
Co	35.8	35.9	20.0	-	28.5	24.5
Ni	32.2	31.5	8.4	-	36.5	40.7
Nb	-	-	-	-	2.4	2.7
Total	100.0	100.0	100.0	100.0	100.0	100.0

Fig. 8. Comparison of the thermal cycle failure mechanism between the double- and triple-layered samples. (a) A backscattered (BSE) image showing the thermal cycled failed double-layered sample and (b) triple-layered sample.
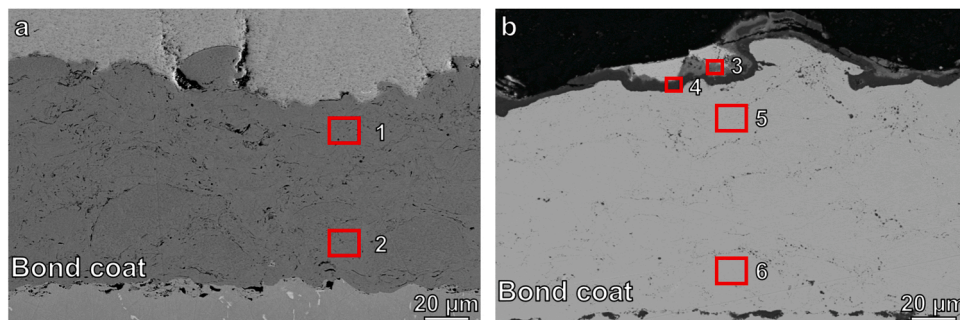

Fig. 9. High magnification of bond coat (a) before thermal cycling and (b) after thermal cycling tests.

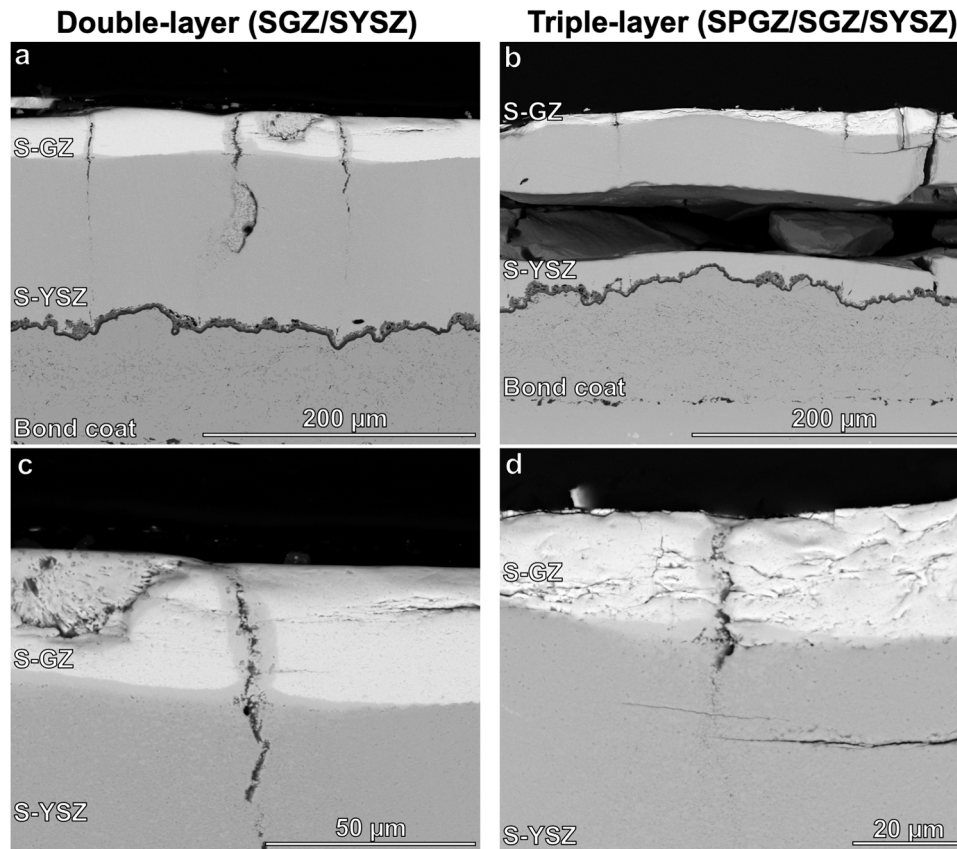**Double-layer (SGZ/SYSZ)**　　　　**Triple-layer (SPGZ/SGZ/SYSZ)**

Fig. 10. Comparison of the CMAS thermochemical test between (a) the double-layered and (b) the triple-layered coatings. A high magnification cross-sectional image for the (c) double-layered coating and (d) triple-layered coating.
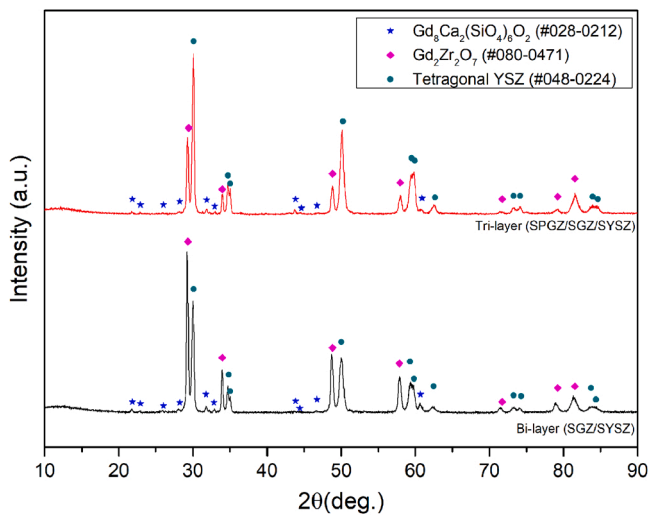

Fig. 11. XRD phase analysis of both the triple- (top) and double-layered (bottom) coatings after CMAS exposure for 0.5 h.

concluded that the formation of DVCs by SP feedstock is mainly contributed by the propagation of microcracks within each splat, in which regions where un-melted particles in close vicinity to the splat boundaries being the favourite crack path, allowing cracks to propagate effortlessly.

Moreover, many lateral cracks are observed to branch out from most DVCs. One of the main factors for forming these lateral cracks is the low fracture toughness of GZ [63,66]. As the deposition process continues, the accumulated stress in the coating is directly proportional to the coating thickness. The propagation of the lateral crack will start as the stress intensity factor exceeds the low fracture toughness value of the GZ [67]. As a result, lateral cracks are seen mainly in the S-GZ. The microcracks or micropores in the coating (i.e., S-GZ) acted as a low energy pathway for the crack to propagate, resulting in the observation of longer lateral cracks in the S-GZ layer. Shinde et al. [23] also reported that the normalised toughness is inversely proportional to the coating thickness. The normalised toughness of the coating dropped below the limiting value for forming the DVCs and lateral cracks, thereby initiating the lateral extension of such independent cracks [23].

4.2. Thermal cycling test

Despite the longer thermal cyclic life of the double-layered sample, the failure mode for both tested coatings were similar, where it occurred at the TGO/topcoat interface. On a side-by-side comparison for both coatings (depicted in Fig. 4), the lower crack density presented in the triple-layer coating could result in being less strain-tolerance capable than the double-layer coating.

In the beginning stage of the thermal cycling test, both samples subjected to the test temperature behaved similarly, where cracks propagated throughout the thickness of TBCs. Due to the microstructure of TBCs (i.e., DVCs, microcracks, and porosities), the surface of the bond coat underwent oxidation in every heating cycle of the test, resulting in the formation of the thermally grown oxide (TGO) layer between the topcoat/bond coat interface. In the meantime, the propagated cracks, or also known as the stress-relieving cracks, also underwent expansion in every heating cycle. Upon cooling, the samples were now undergoing a relaxation state, in which the thermally induced stress in the coating was released in the form of lateral crack propagation, resulting in the branching of horizontal cracks in the topcoat layer. For the TGO layer,
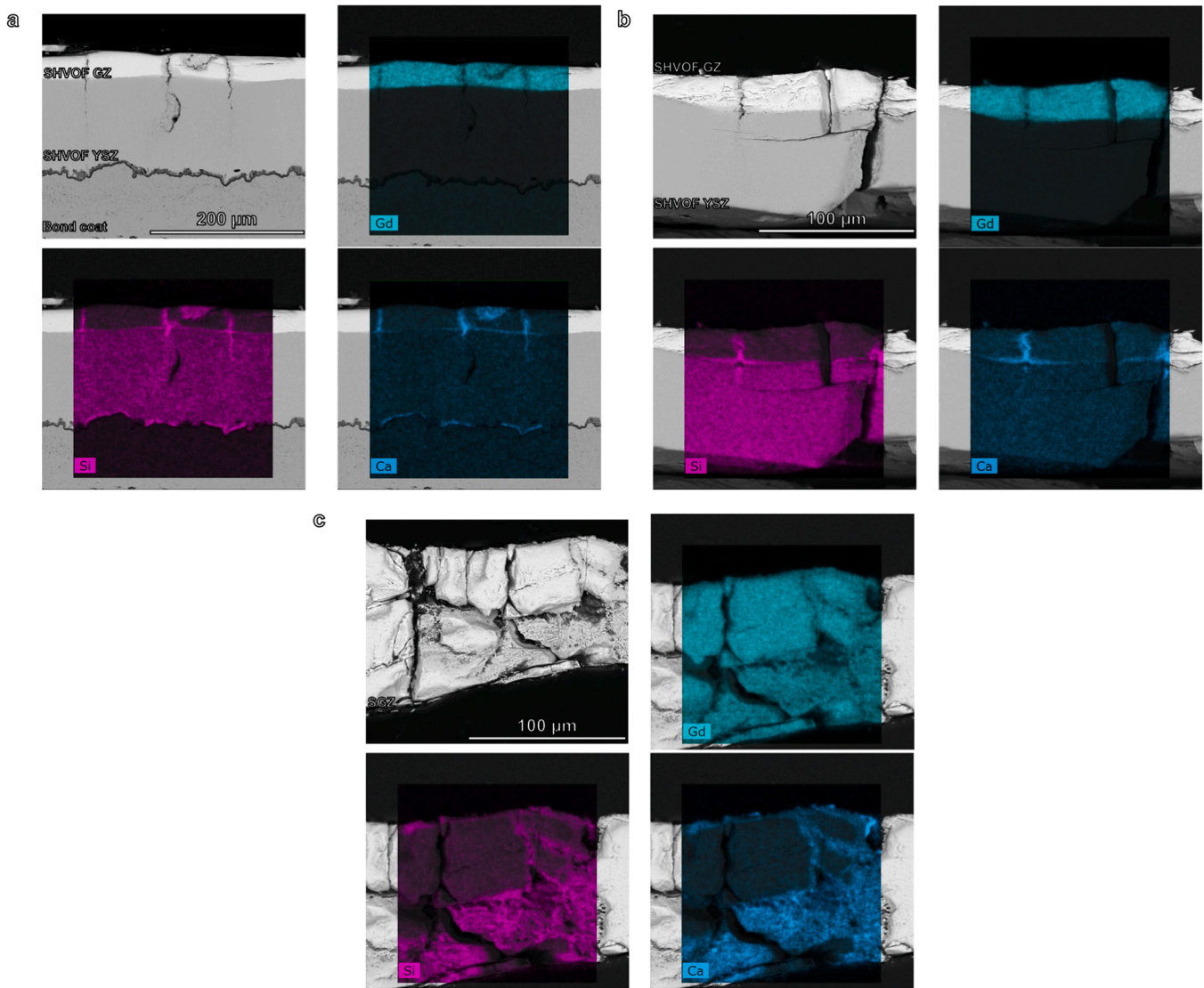
Fig. 12. Elemental maps superposed with BSE image for (a) double- and (b) triple-layered coatings to show the infiltration of CMAS which subsequently led to coating failure. (c) An elemental map of a higher magnification to show the needle-like structure found on the GZ layer.

the stress was relieved by lengthening the TGO layer through out-of-plane displacements, as a result, it was seen as undulated [68]. However, the nucleation of cracks in the TGO layer were mainly attributed to the CTE mismatch between the topcoat and the substrate in the heating and the cooling stage. Naumenko et al. [69] developed an extensive study on the type of cracks that could occur within the TGO layer, leading to the spallation of TBCs. As the number of cycles increased, each of the samples experienced the same cycle, associated with TGO growth and the formation of undesirable oxides after β-phase depletion in the bond coat. Both phenomena (i.e., TGO growth and the formation of undesirable oxides) contribute to the stress accumulation in the TBC system; however, the dominant failure mode for both samples seems to be the lateral crack propagating at the TGO/topcoat interface.

4.3. CMAS test

In the CMAS thermochemical test, the double- and triple-layered coatings failed similarly. Both samples were fully infiltrated with CMAS after exposure for only 0.5 h. It should be noted that in the engine operating conditions, the CMAS exposure onto the surface of TBCs is highly dependent on several factors, such as the flow path of the ingested air, CMAS compositions, the flux of CMAS on the surface of

TBCs and the surface temperature across the hot components [70,71]. In this study, we have tested our samples in controlled laboratory isothermal conditions with an industry-standard flux of CMAS.

In both samples (i.e., double- and triple-layered coatings), the molten CMAS infiltrated the coating structure through DVCs. For the case of the triple-layered coating, the lower crack density existed in the coating structure potentially reduces the open cavities on the surface of the topcoat for the CMAS to infiltrate [72]; however, the smaller opening displacements on the surface of the topcoat (i.e., triple-layer) can be detrimental due to the stronger capillary suction effect. Dictated by the Washburn equation [73], the CMAS infiltration depth in a given time is related to the square-root of the crack width. As studied by Kumar et al. [74], the variation in crack opening displacements is indeed an important factor that affects the CMAS infiltration depth, but several factors such as the speed of apatite formation and CMAS viscosity also should be considered. Also reported by Kumar et al. [19], the width of cracks of less than 1 μm is observed to be sealed by the GZ, in which one can argue that the smaller crack width sealed more easily due to the apatite formation regardless of the high capillary effect. In the current work, the contact angle of the molten CMAS, the widening of crack-opening displacements at elevated temperatures and the viscosity of CMAS at 1250 °C are not known. Hence, a further investigation would be required to

study the CMAS infiltration depth based on these factors.

As soon as the CMAS deposits melted and infiltrated the topcoat, the exposed surface in the GZ layer will undergo a rapid dissolution of GZ upon contact with the melt, subsequently to the nucleation of the apatite phase, $Gd_8Ca_2(SiO_4)_6O_2$, which is evidenced by the needle-like structure found in the GZ layer (Fig. 12) [8]. A similar reaction is also reported by Gildersleeve et al. [72]. In contrast, most of the vertical and horizontal cracks are observed to be sealed by the apatite phase, supported by the reduction of vertical and horizontal cracks in the GZ layer. As the YSZ layer is exposed to the molten CMAS, yttria will be leached out from the metastable tetragonal (t′) YSZ to form Yttria-depleted (Y-depleted) or Yttria-enriched (Y-enriched) zirconia [75]. The Y-depleted zirconia is mainly due to the higher solubility of yttrium in CMAS, leading to the transformation of monoclinic zirconia upon cooling, whereas the Y-enriched zirconia grains are mainly in big round shaped zirconia grains, leading to the transformation of cubic zirconia upon cooling [9, 75]. Some of the zirconia globular grains could be composed of re-precipitated Ca/Si co-stabilised zirconia [75,76]. In the cooling stage, the CMAS infiltrated samples experienced a severe thermal shock behaviour due to the thermal mismatch between the topcoat and the substrate. Moreover, the porosities in the topcoat of both samples reduced significantly, whether attributed to the sintering effect or the CMAS reactant products in the coating [75]. Consequently, the topcoat of both samples underwent a 'shattering' effect.

5. Conclusions

In this work, double-layered and triple-layered TBCs were successfully deposited with the solution precursor and suspension feedstock through the HVOF thermal spray, presenting the typical DVC microstructure that provides the strain-tolerant capability for the thermal cycling test. Instead of altering the spray parameters or conditions, a solution precursor feedstock is used to achieve the dense GZ layer. With the utilisation of SP feedstock, the dense GZ layer altered the dimensions of the DVCs compared to the already deposited suspension layers. The thermal lifecycle for both samples and the CMAS resistance was also studied. The following conclusions can be drawn:

- The double-layered coating shows a better thermal cycling lifecycle than the triple-layered coating. A possible reason for the higher lifecycle in the double-layered coating is the crack density. The double-layered coating had a higher crack density of 10.0 ± 2.0 mm^{-1}, as opposed to the triple-layered coating, 5.5 ± 1.0 mm^{-1}. The higher crack density in the microstructure of TBCs may result in a better strain-tolerance capability. In contrast, the early failure of the triple-layered TBC may be attributed to the high level of stresses accumulated in the TBC system.
- The failure mode of the double- and triple-layered coating are similar. The dominant failure mode for the double- and triple-layered coating occurred at the TGO/topcoat interface. Despite the number of cycles, the bond coat for both thermally cycled samples seems to be fully depleted as no dark contrasted β phase can be observed throughout the thickness of the bond coat. The nominal Al composition throughout the bond coat thickness dropped from ∼ 9 wt% to ∼ 4.5 wt%.
- In the CMAS thermochemical test, both coatings were fully infiltrated by CMAS. Due to the thermal shock behaviour in the cooling stage, both coatings experienced a "shattering effect". Several factors such as contact angle of CMAS, the widening of crack-opening displacements at elevated temperatures and the viscosity of CMAS require further investigation.
- Although multilayer TBCs could be produced through the HVOF thermal spray method, both TBCs (i.e., double- and triple-layer) performed poorly in the isothermal test. For the CMAS test, both coatings were fully infiltrated. The triple-layer coating with a dense SP GZ layer failed to offer resistance against CMAS attack.

Declaration of Competing Interest

The authors declare that they have no known competing financial interests or personal relationships that could have appeared to influence the work reported in this paper.

Acknowledgements

References

[1] R.A. Miller, Thermal barrier coatings for aircraft engines: history and directions, J. Therm. Spray. Techn 6 (1997) 35, https://doi.org/10.1007/bf02646310.

[2] R. Vaßen, M.O. Jarligo, T. Steinke, D.E. Mack, D. Stöver, Overview on advanced thermal barrier coatings, Surf. Coat. Technol. 205 (2010) 938–942, https://doi.org/10.1016/j.surfcoat.2010.08.151.

[3] D.R. Clarke, M. Oechsner, N.P. Padture, Thermal-barrier coatings for more efficient gas-turbine engines, Mrs Bull. 37 (2012) 891–898, https://doi.org/10.1557/mrs.2012.232.

[4] R. Vassen, A. Stuke, D. Stöver, Recent developments in the field of thermal barrier coatings, J. Therm. Spray. Techn 18 (2009) 181–186, https://doi.org/10.1007/s11666-009-9312-7.

[5] X.Q. Cao, R. Vassen, D. Stoever, Ceramic materials for thermal barrier coatings, J. Eur. Ceram. Soc. 24 (2004) 1–10, https://doi.org/10.1016/s0955-2219(03)00129-8.

[6] N.L. NDAMKA, Prof.J.R. Nicholls, MICROSTRUCTURAL DAMAGE OF THERMAL BARRIER COATINGS DUE TO CMAS ATTACK.pdf, Cranfield University, 2014.

[7] M.G. Gok, G. Goller, State of the Art of Gadolinium Zirconate Based Thermal Barrier Coatings: Design, Processing and Characterization, Coatings Technology. (2019).

[8] S. Krämer, J. Yang, C.G. Levi, Infiltration-inhibiting reaction of gadolinium zirconate thermal barrier coatings with CMAS melts, J. Am. Ceram. Soc. 91 (2008) 576–583, https://doi.org/10.1111/j.1551-2916.2007.02175.x.

[9] S. Krämer, J. Yang, C.G. Levi, C.A. Johnson, Thermochemical interaction of thermal barrier coatings with molten CaO–MgO–Al2O3–SiO2 (CMAS) deposits, J. Am. Ceram. Soc. 89 (2006) 3167–3175, https://doi.org/10.1111/j.1551-2916.2006.01209.x.

[10] A.D. Gledhill, K.M. Reddy, J.M. Drexler, K. Shinoda, S. Sampath, N.P. Padture, Mitigation of damage from molten fly ash to air-plasma-sprayed thermal barrier coatings, Mater. Sci. Eng. 528 (2011) 7214–7221, https://doi.org/10.1016/j.msea.2011.06.041.

[11] M. Gupta, Design of Thermal Barrier Coatings - A Modelling Approach, University West, 2014.

[12] S. Mahade, Functional Performance of Gadolinium Zirconate/Yttria Stabilized Zirconia Multi-Layered Thermal Barrier Coatings, University West, 2018.

[13] S. Mahade, N. Curry, S. Björklund, N. Markocsan, P. Nylén, R. Vaßen, Functional performance of Gd2Zr2O7/YSZ multi-layered thermal barrier coatings deposited by suspension plasma spray, Surf. Coat. Technol. 318 (2017) 208–216, https://doi.org/10.1016/j.surfcoat.2016.12.062.

[14] T.M. Pollock, D.M. Lipkin, K.J. Hemker, Multifunctional coating interlayers for thermal-barrier systems, Mrs Bull. 37 (2012) 923–931, https://doi.org/10.1557/mrs.2012.238.

[15] M.G. Gok, G. Goller, Production and characterisation of GZ/CYSZ alternative thermal barrier coatings with multilayered and functionally graded designs, J. Eur. Ceram. Soc. 36 (2016) 1755–1764, https://doi.org/10.1016/j.jeurceramsoc.2016.01.036.

[16] M.G. Gok, G. Goller, Microstructural characterization of GZ/CYSZ thermal barrier coatings after thermal shock and CMAS+hot corrosion test, J. Eur. Ceram. Soc. 37 (2017) 2501–2508, https://doi.org/10.1016/j.jeurceramsoc.2017.02.004.

[17] M. Seraffon, Performances of Air Plasma Sprayed Thermal Barrier Coatings for Industrial Gas Turbines, Cranfield University, 2012.

[18] S.V. Shinde, S. Sampath, Factors governing segmentation crack characteristics in air plasma sprayed ceramics, J. Eur. Ceram. Soc. 42 (2021) 1077–1087, https://doi.org/10.1016/j.jeurceramsoc.2021.10.064.

[19] R. Kumar, D. Cietek, C. Jiang, J. Roth, M. Gell, E.H. Jordan, Influence of microstructure on the durability of gadolinium zirconate thermal barrier coatings using APS & SPPS processes, Surf. Coat. Technol. 337 (2018) 117–125, https://doi.org/10.1016/j.surfcoat.2018.01.004.

[20] J.P. Martins, Y. Chen, G. Brewster, R. McIntyre, P. Xiao, Investigation of the bond coat interface topography effect on lifetime, microstructure and mechanical properties of air-plasma sprayed thermal barrier coatings, J. Eur. Ceram. Soc. 40 (2020) 5719–5730, https://doi.org/10.1016/j.jeurceramsoc.2020.05.082.

[21] J.M. Drexler, C.-H. Chen, A.D. Gledhill, K. Shinoda, S. Sampath, N.P. Padture, Plasma sprayed gadolinium zirconate thermal barrier coatings that are resistant to

damage by molten Ca–Mg–Al–silicate glass, Surf. Coat. Technol. 206 (2012) 3911–3916, https://doi.org/10.1016/j.surfcoat.2012.03.051.

[22] A. Mehta, H. Vasudev, S. Singh, Recent developments in the designing of deposition of thermal barrier coatings – A review, Mater. Today Proc. 26 (2020) 1336–1342, https://doi.org/10.1016/j.matpr.2020.02.271.

[23] S.V. Shinde, E.J.G. V, C.A. Johnson, S. Sampath, Segmentation crack formation dynamics during air plasma spraying of zirconia, Acta Mater. 183 (2020) 196–206, https://doi.org/10.1016/j.actamat.2019.10.052.

[24] Z. Lu, S.-W. Myoung, Y.-G. Jung, G. Balakrishnan, J. Lee, U. Paik, Thermal fatigue behavior of air-plasma sprayed thermal barrier coating with bond coat species in cyclic thermal exposure, Materials 6 (2013) 3387–3403, https://doi.org/10.3390/ma6083387.

[25] G. Boissonnet, C. Chalk, J.R. Nicholls, G. Bonnet, F. Pedraza, Phase stability and thermal insulation of YSZ and erbia-yttria co-doped zirconia EB-PVD thermal barrier coating systems, Surf. Coat. Technol. 389 (2020), 125566, https://doi.org/10.1016/j.surfcoat.2020.125566.

[26] K.S. Lee, K.I. Jung, Y.S. Heo, T.W. Kim, Y.-G. Jung, U. Paik, Thermal and mechanical properties of sintered bodies and EB-PVD layers of Y2O3 added Gd2Zr2O7 ceramics for thermal barrier coatings, J. Alloy Compd. 507 (2010) 448–455, https://doi.org/10.1016/j.jallcom.2010.07.196.

[27] P. Mechnich, W. Braue, U. Schulz, High-temperature corrosion of EB-PVD yttria partially stabilized zirconia thermal barrier coatings with an artificial volcanic ash overlay, J. Am. Ceram. Soc. 94 (2011) 925–931, https://doi.org/10.1111/j.1551-2916.2010.04166.x.

[28] V. Kumar, B. Kandasubramanian, Processing and design methodologies for advanced and novel thermal barrier coatings for engineering applications, Particuology 27 (2016) 1–28, https://doi.org/10.1016/j.partic.2016.01.007.

[29] G. Mittal, S. Paul, Suspension and solution precursor plasma and HVOF spray: a review, J. Therm. Spray. Techn 31 (2022) 1443–1475, https://doi.org/10.1007/s11666-022-01360-w.

[30] M. Yaghtin, A. Yaghtin, P. Najafisayar, Z. Tang, T. Troczynski, Aging behavior of water-based YSZ suspensions for plasma spraying of thermal barrier coatings, J. Therm. Spray. Techn 30 (2021) 97–107, https://doi.org/10.1007/s11666-021-01162-6.

[31] A. Ganvir, N. Curry, S. Björklund, N. Markocsan, P. Nylén, Characterization of microstructure and thermal properties of YSZ coatings obtained by axial suspension plasma spraying (ASPS), J. Therm. Spray. Techn 24 (2015) 1195–1204, https://doi.org/10.1007/s11666-015-0263-x.

[32] A.L. Vasiliev, N.P. Padture, Coatings of metastable ceramics deposited by solution-precursor plasma spray: II. Ternary ZrO2–Y2O3–Al2O3 system, Acta Mater. 54 (2006) 4921–4928, https://doi.org/10.1016/j.actamat.2006.06.026.

[33] K. VanEvery, M.J.M. Krane, R.W. Trice, H. Wang, W. Porter, M. Besser, D. Sordelet, J. Ilavsky, J. Almer, Column formation in suspension plasma-sprayed coatings and resultant thermal properties, J. Therm. Spray. Techn 20 (2011) 817–828, https://doi.org/10.1007/s11666-011-9632-2.

[34] A. Ganvir, N. Curry, N. Markocsan, P. Nylén, F.-L. Toma, Comparative study of suspension plasma sprayed and suspension high velocity oxy-fuel sprayed YSZ thermal barrier coatings, Surf. Coat. Technol. 268 (2015) 70–76, https://doi.org/10.1016/j.surfcoat.2014.11.054.

[35] D. Zhou, O. Guillon, R. Vaßen, Development of YSZ thermal barrier coatings using axial suspension plasma spraying, Coatings 7 (2017) 120, https://doi.org/10.3390/coatings7080120.

[36] S. Mahade, N. Curry, S. Björklund, N. Markocsan, P. Nylén, R. Vaßen, Erosion performance of gadolinium zirconate-based thermal barrier coatings processed by suspension plasma spray, J. Therm. Spray. Techn 26 (2017) 108–115, https://doi.org/10.1007/s11666-016-0479-4.

[37] N. Curry, S. Mahade, A. Venkat, S. Joshi, Erosion performance of suspension plasma spray thermal barrier coatings — A comparison with state of art coatings, Surf. Coat. Technol. 437 (2022), 128311, https://doi.org/10.1016/j.surfcoat.2022.128311.

[38] M. Gell, J. Wang, R. Kumar, J. Roth, C. Jiang, E.H. Jordan, Higher temperature thermal barrier coatings with the combined use of yttrium aluminum garnet and the solution precursor plasma spray process, J. Therm. Spray. Techn 27 (2018) 543–555, https://doi.org/10.1007/s11666-018-0701-7.

[39] W. Algenaid, A. Ganvir, R.F. Calinas, J. Varghese, K.V. Rajulapati, S. Joshi, Influence of microstructure on the erosion behaviour of suspension plasma sprayed thermal barrier coatings, Surf. Coat. Technol. 375 (2019) 86–99, https://doi.org/10.1016/j.surfcoat.2019.06.075.

[40] A. Ganvir, N. Curry, N. Markocsan, P. Nylén, S. Joshi, M. Vilemova, Z. Pala, Influence of microstructure on thermal properties of axial suspension plasma-sprayed YSZ thermal barrier coatings, J. Therm. Spray. Techn 25 (2016) 202–212, https://doi.org/10.1007/s11666-015-0355-7.

[41] R. Jaworski, L. Pawlowski, F. Roudet, S. Kozerski, A.L. Maguer, Influence of suspension plasma spraying process parameters on TiO2 coatings microstructure, J. Therm. Spray. Techn 17 (2008) 73–81, https://doi.org/10.1007/s11666-007-9147-z.

[42] E.H. Jordan, C. Jiang, J. Roth, M. Gell, Low thermal conductivity yttria-stabilized zirconia thermal barrier coatings using the solution precursor plasma spray process, J. Therm. Spray. Techn 23 (2014) 849–859, https://doi.org/10.1007/s11666-014-0082-5.

[43] H. Guo, S. Kuroda, H. Murakami, Microstructures and properties of plasma sprayed segmented thermal barrier coatings, The American Ceramic Society. (n.d.). https://doi.org/10.1111/j.1551–2916.2006.00912.x.

[44] N. Curry, K. VanEvery, T. Snyder, J. Susnjar, S. Bjorklund, Performance testing of suspension plasma sprayed thermal barrier coatings produced with varied suspension parameters, Coatings 5 (2015) 338–356, https://doi.org/10.3390/coatings5030338.

[45] A. Ganvir, S. Joshi, N. Markocsan, R. Vassen, Tailoring columnar microstructure of axial suspension plasma sprayed TBCs for superior thermal shock performance, Mater. Des. 144 (2018) 192–208, https://doi.org/10.1016/j.matdes.2018.02.011.

[46] D. Waldbillig, O. Kesler, The effect of solids and dispersant loadings on the suspension viscosities and deposition rates of suspension plasma sprayed YSZ coatings, Surf. Coat. Technol. 203 (2009) 2098–2101, https://doi.org/10.1016/j.surfcoat.2008.11.027.

[47] C. Jiang, E.H. Jordan, A.B. Harris, M. Gell, J. Roth, Double-layer gadolinium zirconate/yttria-stabilized zirconia thermal barrier coatings deposited by the solution precursor plasma spray process, J. Therm. Spray. Techn 24 (2015) 895–906, https://doi.org/10.1007/s11666-015-0283-6.

[48] C. Jiang, E.H. Jordan, Low Thermal Conductivity YSZ-based Thermal Barrier Coatings with Enhanced CMAS Resistance, University of Connecticut, 2015.

[49] E. Gildersleeve, V. Viswanathan, S. Sampath, Molten silicate interactions with plasma sprayed thermal barrier coatings: role of materials and microstructure, J. Eur. Ceram. Soc. 39 (2019) 2122–2131, https://doi.org/10.1016/j.jeurceramsoc.2019.01.023.

[50] H. Zhao, C.G. Levi, H.N.G. Wadley, Molten silicate interactions with thermal barrier coatings, Surf. Coat. Technol. 251 (2014) 74–86, https://doi.org/10.1016/j.surfcoat.2014.04.007.

[51] R. Wellman, G. Whitman, J.R. Nicholls, CMAS corrosion of EB PVD TBCs: identifying the minimum level to initiate damage, Int J. Refract Met. Hard Mater. 28 (2010) 124–132, https://doi.org/10.1016/j.ijrmhm.2009.07.005.

[52] S. Mahade, R. Li, N. Curry, S. Björklund, N. Markocsan, P. Nylén, Isothermal oxidation behavior of Gd2Zr2O7/YSZ multilayered thermal barrier coatings, Int J. Appl. Ceram. Tec. 13 (2016) 443–450, https://doi.org/10.1111/ijac.12527.

[53] K.L. Leng, A.R. Romero, F. Venturi, I. Ahmed, T. Hussain, Solution precursor thermal spraying of gadolinium zirconate for thermal barrier coating, J. Eur. Ceram. Soc. (2021), https://doi.org/10.1016/j.jeurceramsoc.2021.11.050.

[54] N.P. Padture, M. Gell, E.H. Jordan, Thermal barrier coatings for gas-turbine engine applications, Science 296 (2002) 280–284, https://doi.org/10.1126/science.1068609.

[55] S. Saman, Mircrostructure, oxidation and mechanical properties of as-sprayed and annealed HVOF and VPS CoNiCrAlY coatings, The University of Nottingham, 2010.

[56] M. Bai, H. Maher, Z. Pala, T. Hussain, Microstructure and phase stability of suspension high velocity oxy-fuel sprayed yttria stabilised zirconia coatings from aqueous and ethanol based suspensions, J. Eur. Ceram. Soc. 38 (2018) 1878–1887, https://doi.org/10.1016/j.jeurceramsoc.2017.10.026.

[57] S. Mahade, N. Curry, S. Björklund, N. Markocsan, P. Nylén, Thermal conductivity and thermal cyclic fatigue of multilayered Gd2Zr2O7/YSZ thermal barrier coatings processed by suspension plasma spray, Surf. Coat. Technol. 283 (2015) 329–336, https://doi.org/10.1016/j.surfcoat.2015.11.009.

[58] D. Tejero-Martin, A.R. Romero, R.G. Wellman, T. Hussain, Interaction of CMAS on thermal sprayed ytterbium disilicate environmental barrier coatings: a story of porosity, Ceram. Int (2021), https://doi.org/10.1016/j.ceramint.2021.12.033.

[59] Y. Wang, S. Sun, M. Liu, H. Suo, Study on formation mechanism of YSZ thermal barrier coatings with segmented structure, Aer. Adv. Eng. Res (2015), https://doi.org/10.2991/icadme-15.2015.398.

[60] H. Xu, H. Guo, Thermal barrier coatings, Woodhead Publishing Limited, 2011.

[61] E. Bakan, D.E. Mack, G. Mauer, R. Vaßen, Gadolinium zirconate/YSZ thermal barrier coatings: plasma spraying, microstructure, and thermal cycling behavior, J. Am. Ceram. Soc. 97 (2014) 4045–4051, https://doi.org/10.1111/jace.13204.

[62] A.U. Munawar, U. Schulz, G. Cerri, H. Lau, Microstructure and cyclic lifetime of Gd and Dy-containing EB-PVD TBCs deposited as single and double-layer on various bond coats, Surf. Coat. Technol. 245 (2014) 92–101, https://doi.org/10.1016/j.surfcoat.2014.02.047.

[63] S. Mahade, N. Curry, S. Björklund, N. Markocsan, P. Nylén, Failure analysis of Gd2Zr2O7/YSZ multi-layered thermal barrier coatings subjected to thermal cyclic fatigue, J. Alloy Compd. 689 (2016) 1011–1019, https://doi.org/10.1016/j.jallcom.2016.07.333.

[64] M. Gell, E.H. Jordan, M. Teicholz, B.M. Cetegen, N.P. Padture, L. Xie, D. Chen, X. Ma, J. Roth, Thermal barrier coatings made by the solution precursor plasma spray process, J. Therm. Spray. Techn 17 (2008) 124–135, https://doi.org/10.1007/s11666-007-9141-5.

[65] S. Govindarajan, R.O. Dusane, S.V. Joshi, Understanding the formation of vertical cracks in solution precursor plasma sprayed yttria-stabilized zirconia coatings, J. Am. Ceram. Soc. 97 (2014) 3396–3406, https://doi.org/10.1111/jace.13129.

[66] R. Vaßen, F. Traeger, D. Stöver, New thermal barrier coatings based on pyrochlore/YSZ double-layer systems, Int J. Appl. Ceram. Tec. 1 (2004) 351–361, https://doi.org/10.1111/j.1744-7402.2004.tb00186.x.

[67] S. Mahade, A. Jahagirdar, X.-H. Li, B. Kjellman, S. Björklund, N. Markocsan, Tailoring microstructure of double-layered thermal barrier coatings deposited by suspension plasma spray for enhanced durability, Surf. Coat. Technol. 425 (2021), 127704, https://doi.org/10.1016/j.surfcoat.2021.127704.

[68] A.G. Evans, D.R. Mumm, J.W. Hutchinson, G.H. Meier, F.S. Pettit, Mechanisms controlling the durability of thermal barrier coatings, Prog. Mater. Sci. 46 (2001) 505–553, https://doi.org/10.1016/s0079-6425(00)00020-7.

[69] H. Echsler, V. Shemet, M. Schütze, L. Singheiser, W.J. Quadakkers, Cracking in and around the thermally grown oxide in thermal barrier coatings: a comparison of isothermal and cyclic oxidation, J. Mater. Sci. 41 (2006) 1047–1058, https://doi.org/10.1007/s10853-005-3639-3.

[70] M.P. Borom, C.A. Johnson, L.A. Peluso, Role of environment deposits and operating surface temperature in spallation of air plasma sprayed thermal barrier

coatings, Surf. Coat. Technol. 86 (1996) 116–126, https://doi.org/10.1016/s0257-8972(96)02994-5.

[71] M.P. Borom, C.A. Johnson, L.A. Peluso, Role of environmental deposits in spallation of thermal barrier coatings on aeroengine and land-based gas turbine hardware, V005T13A009-V005T13A009, Manuf. Mater. Metall. Ceram. Struct. Dyn. Control Diagn. Instrum. Educ. Gen. Volume 5 (1996), https://doi.org/10.1115/96-gt-285.

[72] E.J. Gildersleeve, S. Sampath, Dynamic interactions of ingested molten silicate particles with air plasma sprayed thermal barrier coatings, J. Mater. Res 35 (2020) 2321–2334, https://doi.org/10.1557/jmr.2020.196.

[73] E.W. Washburn, The dynamics of capillary flow, Phys. Rev. 17 (1921) 273–283, https://doi.org/10.1103/physrev.17.273.

[74] R. Kumar, S. Rommel, C. Jiang, E.H. Jordan, Effect of CMAS viscosity on the infiltration depth in thermal barrier coatings of different microstructures, Surf. Coat. Technol. 432 (2022), 128039, https://doi.org/10.1016/j.surfcoat.2021.128039.

[75] G. Boissonnet, C. Chalk, J. Nicholls, G. Bonnet, F. Pedraza, Thermal insulation of CMAS (Calcium-Magnesium-Alumino-Silicates)- attacked plasma-sprayed thermal barrier coatings, J. Eur. Ceram. Soc. 40 (2020) 2042–2049, https://doi.org/10.1016/j.jeurceramsoc.2019.12.040.

[76] L. Čelko, D. Jech, S. Tkachenko, P. Komarov, M. Remešová, K. Slámečka, P. Ctibor, Failure of gadolinium zirconate and yttria stabilized zirconia thermal barrier coatings subjected to high temperature calcia-magnesia-alumino-silicate attack, Procedia Struct. Integr. 23 (2019) 360–365, https://doi.org/10.1016/j.prostr.2020.01.113.